Following dynamic nuclear wave packets in N_2, O_2, and CO with few-cycle infrared pulses

S. De,[1,*,†] M. Magrakvelidze,[1] I. A. Bocharova,[1] D. Ray,[1] W. Cao,[1] I. Znakovskaya,[2] H. Li,[1] Z. Wang,[1] G. Laurent,[1] U. Thumm,[1] M. F. Kling,[1,2] I. V. Litvinyuk,[1,3] I. Ben-Itzhak,[1] and C. L. Cocke[1,‡]

[1]*J.R. Macdonald Laboratory, Department of Physics, Kansas State University, Manhattan, Kansas 66506, USA*

[2]*Max-Planck Institut für Quantenoptik, D-85748 Garching, Germany*

[3]*Centre for Quantum Dynamics and Australian Attosecond Science Facility, Griffith University, Nathan, Queensland, Australia 4111*

(Received 30 May 2011; published 10 October 2011)

We study the evolution of nuclear wave packets launched in molecular nitrogen, oxygen, and carbon monoxide by intense 8-fs infrared pulses. We use velocity map imaging to measure the momentum of the ion fragments when these wave packets are interrogated by a second such pulse after a variable time delay. Both quasibound and dissociative wave packets are observed. For the former, measurements of bound-state oscillations are used to identify the participating states and, in some cases, extract properties of the relevant potential-energy surfaces. Vibrational structure is resolved in both energy and oscillation frequencies for the cations of oxygen and carbon monoxide, displaying the same quantum wave-packet motion in both energy and time domains. In addition, vibrational structure is seen in the dication of carbon monoxide in a situation where the energy resolution by itself is inadequate to resolve the structure.

DOI: 10.1103/PhysRevA.84.043410 PACS number(s): 34.50.Rk, 33.80.Rv, 42.65.Ky

I. INTRODUCTION

When an intense laser pulse ionizes (and possibly excites) a molecule on a time scale shorter than the vibrational period, it launches coherent wave packets on one or more potential energy curves (PECs) of the molecular ion. The study of the dynamics of the following motion can yield both insight into molecular dynamics on a femtosecond time scale and, in some cases, can allow the extraction of properties of the active potential surfaces. The use of pump-probe time-resolved spectroscopy to follow the wave-packet dynamics has received considerable study over the past two decades, beginning with the work of Zewail [1]. Available pulse lengths have shortened since the earliest measurements to the point that they are less than the vibrational period of even the lightest diatomic molecule, molecular hydrogen. A number of pump-probe studies of that molecule have now appeared [2–6]. The interpretation is greatly simplified in that case by the fact that the bound-state motion of the molecular cation is dominated by a single-bound potential curve (the $1s\sigma_g$). Similar recent studies of the I_2 molecule, where the propagation times are long and the level structure is tractable, have appeared [7,8]. For more complex molecules, many potential curves are at play, and the observations are more complex to interpret. In an earlier paper [9], we presented a study of molecular dynamics in the dication of oxygen in which we were able to use the observation of vibrational revivals to extract information on the potential-energy curves for several states. In this paper, we present results for the cation and dication of nitrogen, oxygen, and carbon monoxide. We find both dissociative and quasibound wave packets in each system and propose identifications of the channels or states responsible. The most interesting cases occur in molecular oxygen and carbon monoxide for which we find the signature of a single potential-energy surface displayed through both vibrational structure in energy and oscillatory structure in time. Such an observation probes the wave-packet dynamics at the very border of the uncertainty principle where the time-honored energy-resolved vibrational spectroscopy meets, in a single experiment, real-time molecular dynamics.

II. EXPERIMENTAL METHOD

Short (nominally 8-fs) pulses of 800-nm radiation at intensities between 1 and 3×10^{14} W/cm^2 were used to ionize, through strong-field processes, states in the cation of the target molecules. After a time delay of up to 2000 fs, a second similar pulse probed the molecular dynamics. The charge-to-mass ratio and momentum of the fragments were measured using a velocity map imaging (VMI) spectrometer [10,11]. A strong electric field carries the ionic fragments from the interaction of the neutral gas with the laser focus onto the face of a channel-plate chevron followed by a phosphor screen. For each ionic mass, we experimentally isolate the charge of the ion using time-of-flight gating. A two-dimensional projection of the momentum spectrum of the ion is measured (in the x-y plane, with the time-of-flight axis along the z direction). The polarization vector of the laser beam is along the y axis, which results in a cylindrically symmetric momentum spectrum whose projection forms the image. By using a form of inverse Abel transform, we extract the two-dimensional image, which underlies the cylindrical distribution [12]. Further details of the apparatus and data reduction are given in Ref. [9].

III. RESULTS

A. General comments

We use a brief summary of the case of molecular hydrogen as a starting point [2–6]. For H_2 (or D_2), the pump pulse, by removal of the outermost electron of the highest occupied molecular orbital (HOMO) from the neutral molecule,

*Present address: Department of Chemistry, Aarhus University, DK-8000 Aarhus C, Denmark.

†sankar@phys.ksu.edu

‡cocke@phys.ksu.edu

launches a wave packet on the potential curves of the cation. If this curve is dissociative ($2p\sigma$ for hydrogen), the packet proceeds monotonically outward, producing, at an internuclear distance (R) of infinity, one charged and one neutral fragment. If this process is interrupted after some delay by the probe pulse, which removes the remaining electron, the system Coulomb explodes, with a final kinetic-energy release (KER), which is primarily (but not exclusively) a measure of the wave-packet probability density as a function of R, reflected onto the Coulomb PEC for two protons. On the other hand, if the PEC of the parent has a potential well in the Franck-Condon (FC) region ($1s\sigma$), the wave packet will oscillate in the well. With the arrival of the probe, the same reflection mapping of R onto the KER through the two-proton PEC occurs. The motion of the bound wave packet is revealed through an oscillation with delay time (τ) of the KER. In fact, both the KER and the total yield in the Coulomb explosion channel oscillate with τ because of the strong dependence of the ionization efficiency of the probe pulse on the internuclear distance.

1. What is different for multielectron diatomics?

(1) First, the excitation mechanisms are less straightforward. In strong-field ionization of multielectron molecules, the most probable first step is the removal, by tunneling, of one electron from the HOMO of the neutral. Removal of the HOMO from neutral oxygen, nitrogen, or carbon monoxide results in the population of low-vibrational states of the ground state of the cation. These states are bound with no direct dissociation. If further excitation of the cation occurs, through rescattering excitation, extraction of electrons from inner orbitals, bond softening, or sequential ionization or excitation, dissociative states of the cation and higher charge states can be populated. As we discuss in more detail later, it is quite possible that extraction of the HOMO-1 or even HOMO-2, followed by bond softening will be an important contributor to the production of dissociative states of the cation. Experimentally, considerable population of dissociative wave packets is seen.

(2) Second, many different charge states of the parent molecular ion can be created by the pump pulse, and, for each of these, wave packets are launched on many different PECs simultaneously (coherently). In order to identify the states responsible for the subsequent wave-packet motion, a carefully focused analysis of the oscillation and vibrational revival periods of the bound-state wave packets is needed.

(3) Third, many different charge states of the final ion are created by the probe, and no unique final state for the Coulomb dissociation is created, unlike the case for molecular hydrogen where only the PEC for proton pairs results. Thus, the interpretation of the KER as a reflection of the spatial wave function seen by the probe is no longer unique.

Figure 1 shows inverted VMI images for N^+, O^+, and C^+ ions resulting from the fragmentation of N_2, O_2, and CO, respectively. A recent cold-target recoil-ion momentum spectroscopy (COLTRIMS) pump-probe study of molecular oxygen and nitrogen [13], for which the charge states of both final fragments were determined experimentally, shows a strong grouping of the final momenta according to charge state. In this paper, we measure only one charged fragment.

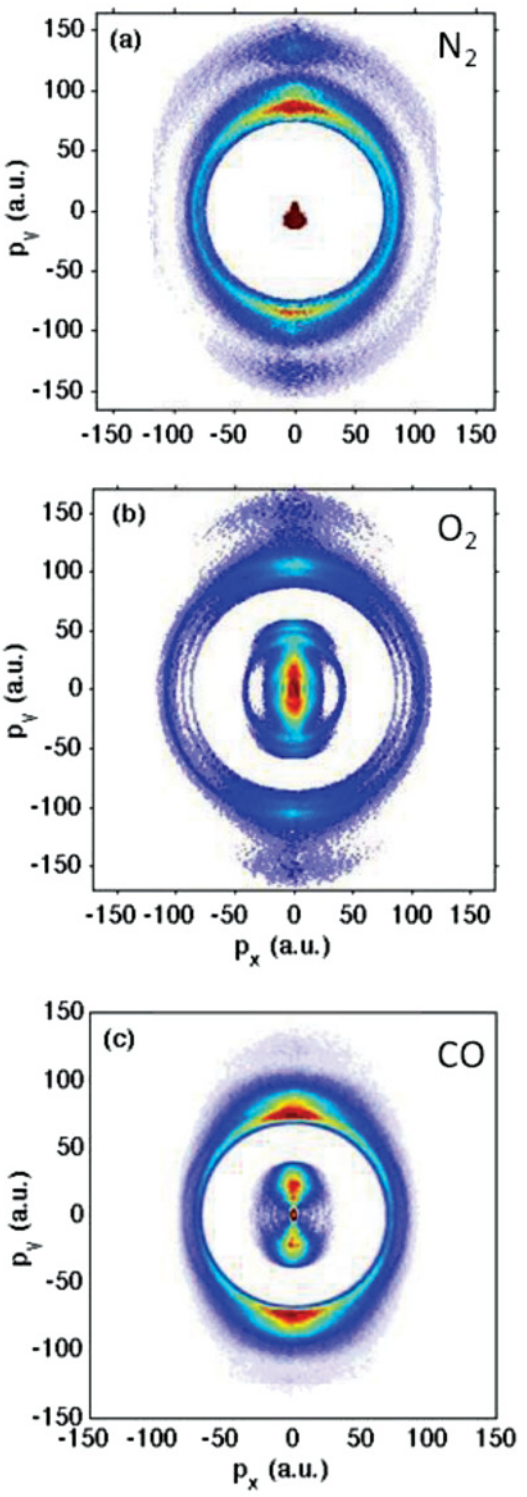

FIG. 1. (Color online) Inverted momentum images for detected (top to bottom) (a) N^+, (b) O^+, and (c) C^+ ions from N_2, O_2, and CO, respectively at the pump-probe delay of 500 fs.

Fortunately, the magnitude of the momentum of the fragment is usually sufficient to identify the charge of the other fragment. For example, the images in Fig. 1 typically show an inner group, corresponding to N^+/N, O^+/O, and C^+/O, respectively, surrounded by a second group corresponding

to N^+/N^+, O^+/O^+, and C^+/O^+, respectively. Also, a much weaker outer ring corresponding to N^+/N^{2+}, O^+/O^{2+}, and C^+/O^{2+} is seen. The VMI has the advantage in that a much denser target can be used than for COLTRIMS experiments, and thus, spectra with high statistics over a very long range of delay times can be obtained.

B. Dissociative states

We discuss the dissociative states and bound states separately. Dissociative states of the parent ion, which give rise to wave packets centered at internuclear distances that increase monotonically with time, produce slowly descending stripes when exposed to the time-dependent probe. In Fig. 2, we show plots of the KER, deduced from the measured momentum spectra, as a function of τ for the observation of doubly charged oxygen and nitrogen ions. We identify the origins of dissociative wave packets for each case by superimposing the expected KER-vs-τ curves calculated classically [13] for each case. The calculated curves are deduced by assuming that the potential curves of both the parent molecule and the final molecule are purely Coulombic. Apart from the choice of charge-state combinations, the only adjustable parameter in the calculation is the asymptotic KER of the parent ion (the KER that would occur if no probe pulse appeared). For the oxygen case [Fig. 2(a)], curves 1–4 can be identified as: (1) dissociating states of the cation to O^+/O with an asymptotic KER of 1 eV, ionized by the probe pulse to O^{2+}/O^+; (2) the same state ionized to O^{2+}/O^{2+}; (3) dissociating states of the dication to O^+/O^+ with an asymptotic KER of 7.5 eV [14], ionized by the probe pulse to O^{2+}/O^+; (4) the same state ionized by the probe pulse to O^{2+}/O^{2+}. For the nitrogen case, curves 1 and 2 are identified as (1) dissociating states of the dication to N^+/N^+ ionized by the probe pulse to N^{2+}/N^+ with a KER of 7.5 eV [14] and (2) the same states ionized to N^{2+}/N^{2+}. For very small R, the exact shape of each trajectory is dependent on the exact shape of the PECs for both parent and final molecular ions. We do not attempt to interpret this here, however, since the extraction of such information is very difficult from dissociative paths alone. Generally speaking, the dissociation occurs in the direction of the laser polarization and partially obscures the bound-state wave-packet motion. For this reason, when we are interested in the motion of the bound-state wave packets, we usually choose to select ions emitted perpendicular to the polarization vector.

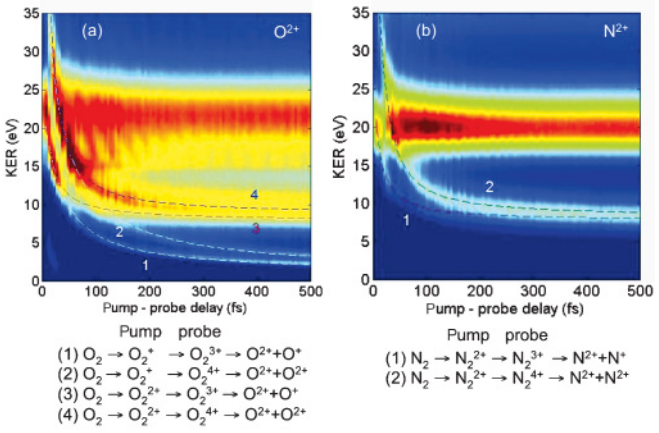

FIG. 2. (Color online) A plot of the KER vs pump-probe delay for (a) O^{2+} and (b) N^{2+} ions. The descending curves correspond to the population of the parent and final molecular ions indicated in the legend. The dashed curves were calculated from the Coulombic model discussed in the text.

C. Bound (or quasibound) states

For the purposes of this discussion, any wave packet that is confined in a well for several hundred femtoseconds or more will appear as a bound wave packet. Since the internuclear distance is relatively localized by the binding well, the KER, as a function of time, will appear as a band at some average KER value, determined roughly by the charge states of the final ions. Within this band, the details of the wave-packet motion will appear as a fine structure. For each parent PEC, the resulting wave packet is formed from a coherent combination of vibrational states whose sum, at $\tau = 0$, is approximately the ground-state vibrational wave function of the neutral molecule. As time progresses, these different vibrational states beat against each other to produce the subsequent wave-packet motion. Several PECs are likely to be populated together. We focus our attention on those formed from the extraction of the HOMO, the HOMO-1, and sometimes, the HOMO-2 from the neutral molecule, which proves to be adequate for the interpretation of most of our spectra. The motion of the wave packet on each PEC is approximately harmonic in nature, with a classical oscillation period given by Planck's constant divided by the vibrational energy spacing for the active vibrational states [15]. This period is slightly dependent on the vibrational quantum number (ν) because the well is never purely harmonic. Including anharmonicity, the vibrational energies for a given PEC can be written in terms of the dimensionless anharmonicity parameter x as (Unless specified otherwise, we use atomic units with $e = m = \hbar = 1$)

$$E(\nu) = E_0 + \omega_0(\nu + 1/2) - \omega_0 x(\nu + 1/2)^2, \qquad (1)$$

and the angular oscillation frequency $\omega(\nu)$, which represents the beat between levels ν and $\nu + 1$, is given by

$$\omega(\nu) = \omega_0 - 2\omega_0 x(\nu + 1). \qquad (2)$$

This motion can be seen in the pump-probe experiment through any of several mechanisms, which are neither simple nor sure to identify. Some of the possibilities include:

(1) If the probe pulse ionizes the parent system further to a higher charge-state final molecule, the KER will reflect the R-dependent shape of the bound wave packet at the time of the probe, as in the case of molecular hydrogen. Because the efficiency for this process is strongly R dependent, both the KER and the total yield will oscillate with the period of the wave packet.

(2) If the parent ion has a weak coupling to a dissociative curve through a crossing with a predissociation state, the probe pulse can alter the effective strength of this coupling when the wave packet passes through the crossing. For example, if the presence of the probe should increase the coupling, the yield of final ions will be enhanced when the packet passes this crossing, and the yield of ions will oscillate with the oscillation period of the parent wave packet.

(3) If the parent ion can be promoted by resonant absorption of a single photon (bond softening [16,17]) to a dissociative final state of the same charge state, the yield of the final ion will be enhanced each time the wave packet passes through the resonance region. In this case, different vibrational states of the parent ion wave packet will be promoted to different energies on the dissociative curve, resulting in a correlation between the vibrational state and the KER. The yield will again oscillate with the period of the parent wave packet, and the period will vary slightly with the vibrational quantum number v in the parent ion (beating between v and $v+1$) and, thus, the KER in the final ion.

The tools at our disposal, in trying to identify the source of the beat patterns, include not only the oscillation frequency but also the vibrational revival time, given by $T_{\text{revival}} = \pi/\omega_o x$ [15,18–20], which we observe in several cases and reported earlier for the dication of oxygen [9]. In addition, we compute the power spectrum introduced in references [20] and [21] as a density plot of ion yield versus the quantum-beat frequency and the KER. The power spectrum is obtained by Fourier transformation over a finite time interval of the time-delay-dependent KER spectrum. Such a power spectrum has proven quite useful in the identifications [9,21,22]. Below, we present results for each target species separately.

1. Nitrogen

Removal of the $3\sigma_g$ HOMO from the neutral molecule will result in population mainly of the $X\ ^2\Sigma_g^+$ ground state of the cation; removal of the HOMO-1 ($1\pi_u$) produces the $A\ ^2\Pi_u$ state (see Fig. 3). The minimum and curvature of the PEC of the $X\ ^2\Sigma_g^+$ state are almost the same as those for the neutral nitrogen, which means that a wave packet launched into this well will populate only the first few vibrational states and will oscillate only weakly.

In Fig. 4(a), we show a plot of KER vs τ for the observation of the N^{2+} fragment. The broad stripes near the KER of 20 and 40 eV corresponds to the motion of wave packets in the cation and dication parent systems, ionized by the probe pulse to N^+/N^{2+} and N^{2+}/N^{2+}, respectively. A projection of the

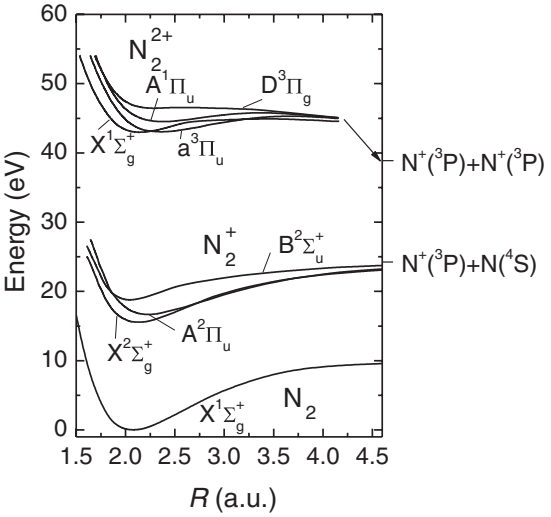

FIG. 3. Partial energy-level scheme for N_2, N_2^+, and N_2^{++}. Adapted from Refs. [23–25].

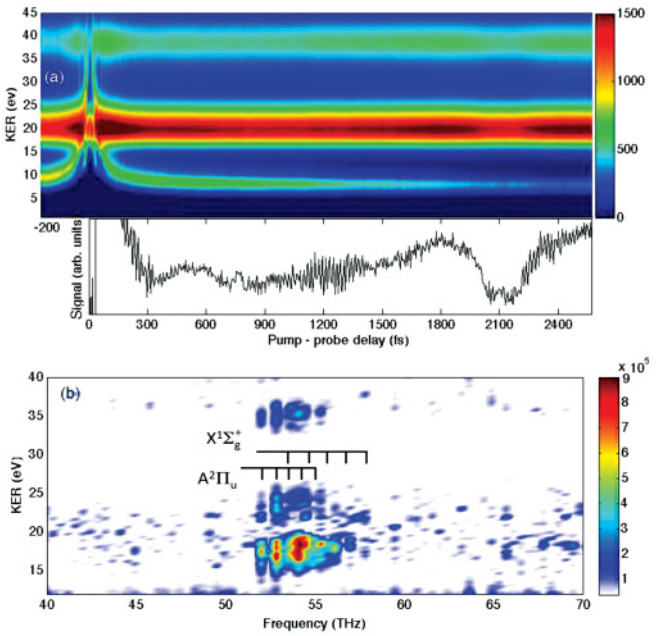

FIG. 4. (Color online) (a) KER vs τ for N^{+2} ions emitted at $\pm 30^\circ$ to the polarization vector. The lower panel shows a projection of the 20 (± 1) eV band. (b) Power spectrum of (a). The vibrational combs for the $X\ ^1\Sigma_g^+$ state of N_2^{2+} and the $A\ ^2\Pi_u$ state of N_2^+ are indicated.

20 (± 1) eV band onto the time axis is shown in the lower panel of Fig. 4(a). The projection shows oscillatory motion with a period near 18 fs and a revival near 1200 fs. The first quarter-rotational revival of the neutral molecule [26] is visible at 2100 fs, the main observable motion of the neutral molecule. Figure 4(b) shows the power spectrum for the KER between 13 and 40 eV.

In Table I, we list the known spectroscopic properties for several states in the cation and dication of the molecules used in this experiment. While the extraction of the HOMO in nitrogen, producing the $X\ ^2\Sigma_g^+$ state, would be expected to be strong, this state would produce a group extending below 65 THz in Fig. 4(b) and is not seen; the wave packet does not oscillate. On the other hand, extraction of the HOMO-1 populates the $A\ ^2\Pi_u$ state, and evidence for this state is clear in Fig. 4(b). Furthermore, the expected revival time for this state is 1100 fs, close to the observed revival at 1200 fs seen in Fig. 4(a). Thus, the identification of the oscillations for nitrogen seems to be on solid footing. The distribution of the KER in Fig. 4(a) for this state results from the probe populating several different final states. While it is possible that states of the dication could also contribute in this spectrum, as was found for oxygen [9], the frequencies for the known probable states of the dication do not match the observed spectrum (see Table I). We show, for comparison, the expected frequencies for the ground state of the dication, the $X\ ^1\Sigma_g^+$; there is no strong evidence for this state.

2. Oxygen

Here, we concentrate on the low-KER part of the oxygen spectrum (higher-KER features were discussed in Ref. [9]). Figure 5(a) shows a plot of the KER vs τ spectrum for the KER below 2 eV, where we have chosen ions detected

TABLE I. Spectroscopic constants for molecular states discussed in the text.

Ion	State	ω_o (eV)	x	ν_o (THz)	T_{osc} (fs)	T_{revival} (fs)	References
N_2^+	$X\,^2\Sigma_g^+$	0.274	0.00757	66.228	15.099	998	[27]
	$A\,^2\Pi_u$	0.233	0.00806	56.372	17.739	1101	
N_2^{++}	$X\,^1\Sigma_g^+$	0.247	0.01396	59.792	16.725	599	[28]
	$a\,^3\Pi_u$	0.185	0.01309	44.674	22.385	855	
	$A^1\Pi_u$	0.175	0.01758	42.201	23.696	674	
O_2^+	$a\,^4\Pi_u$	0.128	0.01003	31.058	32.198	1605	[29]
	$A\,^2\Pi_u$	0.111	0.01511	26.935	37.126	1229	
CO^+	$X^2\Sigma^+$	0.277	0.00714	67.098	14.904	1044	[30]
	$A^2\Pi$	0.190	0.00734	45.836	21.817	1486	
	$B\,^2\Sigma^+$	0.213	0.01396	51.570	19.391	695	
CO^{++}	$X^3\Pi$	0.184	0.01998	44.518	22.463	562	[31]
	$^1\Pi$	0.189	0.01270	45.665	21.898	862	
	$^3\Sigma^+$	0.270	0.03704	65.296	15.315	207	

$\pm 30^\circ$ perpendicular to the polarization vector. Evidence for oscillatory structure is immediately apparent. Furthermore, evidence for the vibrational structure of the lower-energy group is also apparent, as can be seen from the projection of the yield onto the energy axis shown in Fig. 5(b). The product of the energy spacing (approximately 0.12 eV) and the oscillation period (approximately 34 fs) is 4.1×10^{-15} eV-seconds, which is Planck's constant. Thus, these features are to be associated with the same physical phenomenon, revealed both in the time domain and in the spectral domain. That it is possible to see both in a single spectrum, at first, might seem surprising. If the pulse length is too long, one would not expect to be able to see the time structure because of the lack of time resolution; on the other hand, if the pulse length is too short, one would not expect to be able to see the energy structure because the broad bandwidth would result in a lack of energy resolution. Apparently, in this case, the pulse structure is such that both are visible in the same spectrum. The oscillation period increases slowly as the KER increases, resulting in a series of lines, which tilt increasingly to the right as the delay increases. This is quite different from the behavior of the vibrational wave packets seen in molecular hydrogen (process (1) above [2–6,18]), where the shape of the oscillatory features is determined by the reflection of the wave packet onto a highly repulsive dissociative curve. In the present case [process (3) above], the shape of the stripes is determined by the chirp of the wave packet itself: higher vibrational states, which correspond to higher KER release, have closer vibrational spacings, and thus, the oscillation beating period, determined by the vibrational energy-level spacing, is longer (see also Ref. [32]).

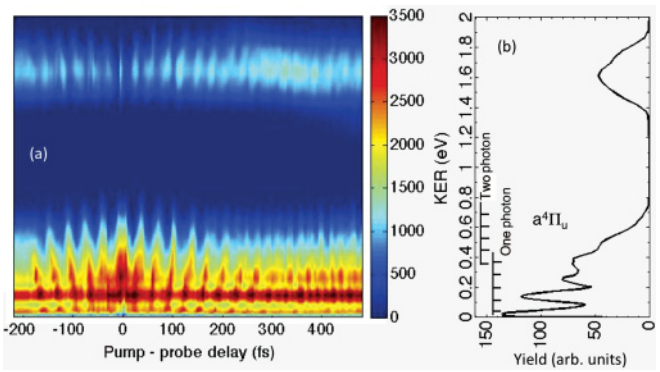

FIG. 5. (Color online) (a) Density plot of the yield of O^+ ions as a function of the KER and delay time for the low-KER region. (b) Projection of the spectrum onto the KER axis. The expected vibrational combs for the $a\,^4\Pi_u$ state are shown for one- and two-photon absorptions from the probe beam, with the lowest vibrational quantum number being $\nu = 11$ and 0, respectively. See text.

Vibrational structure in the KER spectra of H_2 has been seen previously [33–36] for bond softening of H_2^+ beams. The structure is pronounced when pulses long enough to have a narrow bandwidth (21 fs yields a bandwidth of 100 meV) are used. The basic process is photoionization of the vibrational states of the $1s\sigma_g$ PEC of H_2^+. In order to maintain the vibrational energy resolution, it is important that the process be single photon or possibly two photon, since any transition involving a large number of photons would not have the bandwidth to resolve vibrational structure. Similar vibrational structure has been seen recently by Zohrabi *et al.*. [37] in experiments carried out on the strong-field ionization of O_2^+ beams. In that case, the ion beam was composed of both the $X\,^2\Pi_g$ ground state and the $a\,^4\Pi_u$ excited state, with an incoherent vibrational state distribution. The $a\,^4\Pi_u$ state can be promoted by a single photon into the O^+/O continuum through coupling with the $f\,^4\Pi_g$ state, and the energy structure was attributed to the vibrational structure of the $a\,^4\Pi_u$ state. When one starts with neutral O_2, as is the case in this paper, the extraction of an electron from the π_g HOMO of O_2 will result in the population of a weakly vibrating wave packet on the $X\,^2\Pi_g$ potential curve, which can only yield low-energy O^+ ions through multiple-photon processes, while extraction from the $3\sigma_g$ HOMO-1 will result in more strongly vibrating wave packets on the $a\,^4\Pi_u$ and $A\,^2\Pi_u$ curves (see Fig. 6), which can easily be fragmented by absorption of a single additional photon. Since the $a\,^4\Pi_u$ lies lower, it is expected to be more strongly populated. As shown in Fig. 6(b), a single-photon transition from the $a\,^4\Pi_u$ can reach unbound states, through coupling with the $f\,^4\Pi_g$ potential curve, if the initial vibrational

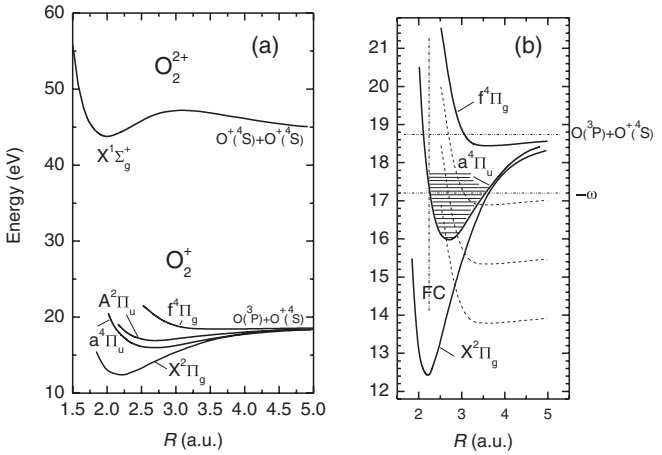

FIG. 6. (a) Selected PECs for O_2 and O_2^+. (b) A detailed view of the process, whereby the $a\ ^4\Pi_u$ state populated by the pump is pumped by a single- or double-photon absorption to the $f\ ^4\Pi_g$ state by the probe and dissociated to O^+/O. The FC region is denoted. See text for details. Adapted from Refs. [25,38].

quantum number is near $\nu = 11$ or higher (the bond-softening crossing), and low-energy O^+ ions are produced. We suggest that the $a\ ^4\Pi_u$ is produced initially by the pump pulse, and the subsequent single-photon absorption is generated by the probe, giving rise to the observed oscillatory yield of the low KER O^+ ions with time. The expected KER, as a function of ν, deduced simply from energy conservation, is shown in Table II. The vibrational frequencies are calculated from the PEC of Marian *et al.* [38]. A two-photon transition from the $a\ ^4\Pi_u$ state would have sufficient energy or fragment states with lower vibrational quantum numbers, and the corresponding energies for this process (above-threshold dissociation [16,17]) are also shown in Fig. 5(b).

The motion of the wave packet observed in Fig. 5 is chirped: the oscillation frequency becomes slower as the KER increases. Indeed, the energy and time structure we observe here place much more demanding constraints on the mechanism than either one alone would. For a single photon absorbed from the probe, each vibrational state ν in the $a\ ^4\Pi_u$ well will beat with the state with $\nu + 1$ to produce the oscillation frequency given by Eq. (2). Similarly, each ν will produce a single KER from energy conservation. Table II shows the corresponding frequencies and KER values for each ν. The situation is similar to the well-known bond-softening and above-threshold dissociation processes in molecular hydrogen [16,17], except that, because the $f\ ^4\Pi_g$ dissociating state is nearly flat beyond 3 a.u., vibrational states that result in even slightly positive KER asymptotically can be populated through the $f\ ^4\Pi_g$ state. In the case of hydrogen, the dissociative state $(2p\sigma)$ is substantially repulsive in the interesting region of internuclear distance, and promotions onto this curve appear at infinity boosted by the corresponding potential energy of this curve.

This chirp of the wave packet is particularly clear in the power spectrum. Figure 7 shows such a spectrum, KER vs frequency, obtained from the Fourier transform of a temporal measurement similar to Fig. 5(b) but extending out to $\tau = 1.2$ ps. The series beginning near a KER of zero and 32 THz we attribute to the production of the $a\ ^4\Pi_u$ by the pump, followed by field-free oscillation and then fragmentation through the $f\ ^4\Pi_g$ following one- or two-photon absorption from the probe. The expected positions from Table II for this sequence are shown as full dots in Fig. 7(a). If the one-photon process was dominant, the calculated vibrational frequency for $\nu = 11$ and higher would be 23 THz and lower. The trend is very similar to the data, with the correct slope in the KER-frequency space and the correct spacing in both KER and frequency. From

TABLE II. Calculated oscillation frequencies and KER values for selected states in the cation and dication of O_2 and CO. For the dication states of CO, the frequencies were calculated by fitting the energies given by Lundqvist *et al.*. [31] to Eq. (1) and using Eq. (2). For the cation states, the KER values are calculated on the assumption of single-photon absorption, as described in the text.

State	ν	ν_n (THz)	KER (eV)	References
$O_2^+\ a\ ^4\Pi_u$	0	31.34	−1.187	[38]
	1	30.60	−1.059	
	2	29.86	−0.934	
	3	29.12	−0.812	
	4	28.38	−0.694	
	5	27.64	−0.578	
	6	26.90	−0.465	
	7	26.16	−0.356	
	8	25.42	−0.249	
	9	24.68	−0.146	
	10	23.94	−0.046	
	11	23.19	0.051	
	12	22.45	0.146	
	13	21.71	0.237	
	14	20.97	0.325	
	15	20.23	0.410	
$CO^+\ B\ ^2\Sigma^+$	6	41.49	0.127	[30]
	7	40.05	0.299	
	8	38.61	0.465	
	9	37.17	0.624	
	10	35.73	0.778	
	11	34.29	0.926	
	12	32.85	1.067	
$CO^{++}\ X\ ^3\Pi$	0	44.86	5.286	[31]
	1	42.74	5.472	
	2	40.62	5.649	
	3	38.50	5.817	
	4	36.38	5.976	
	5	34.25	6.126	
	6	32.13	6.268	
$CO^{++}\ ^1\Pi$	0	44.35	5.839	[31]
	1	43.23	6.023	
	2	42.10	6.201	
	3	40.98	6.376	
	4	39.85	6.545	
	5	38.73	6.710	
	6	37.60	6.870	

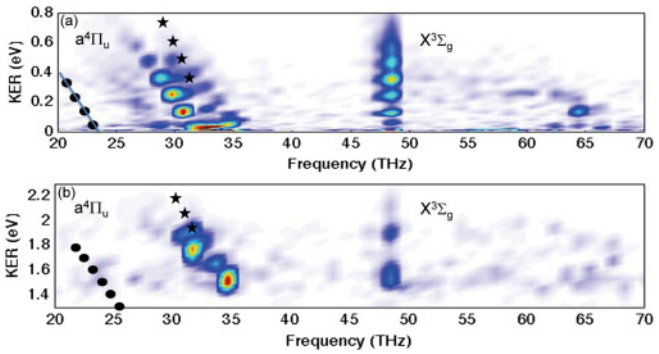

FIG. 7. (Color online) (a) Power spectrum for the KER region below 1 eV. Expected loci for the frequency-KER for one- and two-photon absorption by vibrational states of the $a\,^4\Pi_u$ state are shown as dots and stars, respectively. The short line segment is from Eq. (3), evaluated for $v = 11$. (b) Similar to (a) but for the 1.3–2.3 eV KER range. See Table II and text.

Eqs. (1) and (2), it can be shown that the slope $\Delta E/\Delta f$ of this line is given by

$$\Delta E/\Delta f = h/2[1/x - 2(v+1)] = 4.1 \times 10^{-3}\,\text{eV/THz}[1/x - 2(v+1)] \quad (3)$$

where h is Planck's constant and v is the vibrational quantum number for which the slope is evaluated. This slope is mainly determined by the anharmonicity parameter x. By following events along this line, with sufficient resolution in either f or E, one can determine the spacing of the other parameter. Short line segments are shown in several of our KER-frequency plots. For example, in the present case of Fig. 7(a), the resolution of the vibrational structure in energy is superior to that in frequency, although separate islands are clearly seen in both directions when the data are plotted in the KER-f space. The observed slope for the $a\,^4\Pi_u$ state is in agreement with the data, but the exact location of the line is not. Nevertheless, we believe that we have probably correctly identified the basic process.

We explore the possibility that the observations correspond to absorption of two photons from the probe, rather than one. This process would add 1.55 eV of the KER to each vibrational state in Table II and would result in the starred points shown in Fig. 7(a). The frequencies are higher because this additional KER allows $v = 0$ to be ionized, and the states with lower vibrational quantum numbers have higher oscillation frequencies [see Eq. (2)]. Thus, the predicted frequencies for the two-photon process are closer to the observed data, but the KER progression does not fit well. Furthermore, in the data, we would expect to see both one- and two-photon processes. We know of no way to explain how we would observe the two-photon process only.

A second KER peak appears in Fig. 5(b) about 1.5 eV higher than the low-energy group. The power spectrum for this group is shown in Fig. 7(b) and is similar to that for Fig. 7(a). We interpret Fig. 7(b) to come from the same process as that responsible for Fig. 7(a) but with one additional photon added. Again, the dots in that figure show the expected locations for the net two-photon process and for the same process with one additional photon added (stars). The comparison suffers in exactly the same way as that for Fig. 7(a). Qualitatively, it is very similar to the data, but the frequencies predicted are too low.

Both power spectra in Fig. 7 show a strong group near 48 THz. This frequency is in good agreement with the expected $v = 0$ to 1 frequency in the well of the neutral O_2 ground state. We believe this feature is caused by the launching of a wave packet in the neutral molecule by the pump, possibly through a "Lochfrass" process [39], and that the role of the probe is to ionize this wave packet to the $a\,^4\Pi_u$ state. Since there is no further probe to dissociate this wave packet, we suspect that the weak wings of the probe pulse could nevertheless provide sufficient coupling to dissociate the $a\,^4\Pi_u$ wave packet after it has traversed the well a few times, leading still to the vibrational structure of the $a\,^4\Pi_u$ state. Because the oscillation period is determined by a different PEC from that which ultimately determines the vibrational energy structure, there is no longer a correlation between the frequency and the KER, resulting in a vertical line in Fig. 7. Finally, in Figs. 7(a) and 7(b), there is some evidence for $\Delta v = 2$ oscillations in the a $^4\Pi_u$ well near 65 THz, which is to be expected.

3. *Carbon monoxide*

Carbon monoxide displays two regions of interest in the KER spectrum, shown in Fig. 8. The higher KER group between 5 and 9 eV corresponds to the fragmentation of the dication into C^+ and O^+. There are many dissociative states contributing (see Fig. 9 for a partial schematic of the CO cation and dication curves). The states that were observed by Lundqvist *et al.* [31] to produce observable vibrational series and, thus, likely to generate bound wave packets, are indicated by vibrational combs in Fig. 8. A number of other dissociative states may contribute as well in this region [28,44].

Figure 10(a) shows the KER vs τ for this group of states, with the power spectrum in Fig. 10(b). Clear oscillations are seen in Fig. 10(a) with a period near 25 fs and a vibrational revival near 560 fs. Other revivals occurring near 1190 and

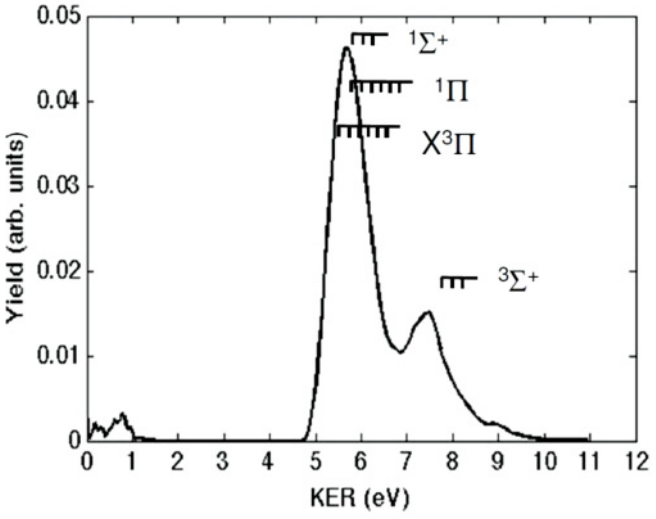

FIG. 8. The KER spectrum for the observation of C^+ ions from CO. The vibrational states identified by Lundqvist *et al.* [31] are indicated in the figure. The data are from a $\pm 15^\circ$ slice perpendicular to the polarization vector.

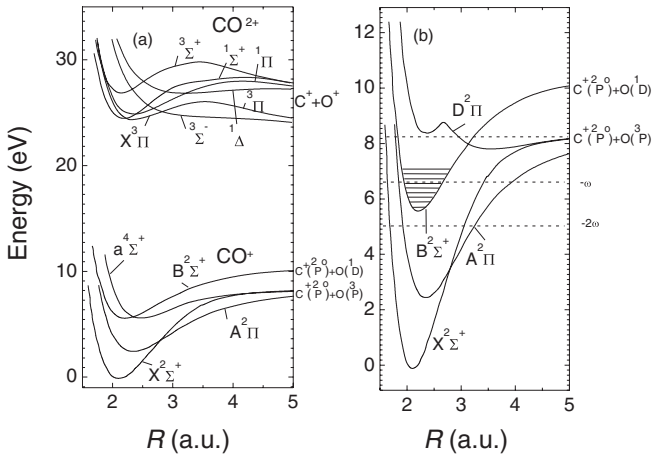

FIG. 9. (a) Partial PECs for cation and dication CO molecules. (b) Expanded schematic for the coupling of the $B\,^2\Sigma^+$ state to the first dissociative limit of the dication. Adapted from Refs. [30,31,40–43].

1800 fs are attributed to higher orders of the 560-fs revival. The expected properties for several wells in the dication and cation are shown in Table I. We believe these structures in Fig. 10(a) are due mainly to oscillations in the $X\,^3\Pi$ ground-state well of the dication. The predicted revival time of 561 fs is in excellent agreement with the observed revival at 560 fs.

Figure 10(b) shows these data in the form of a power spectrum. We attribute the features near 40 THz to oscillations mainly in the $X\,^3\Pi$ well with some contributions from the $^1\Pi$ as well. The solid dots superimposed on the data in Fig. 10(b) are the KER values taken from Linqvist *et al.* [31] and plotted as a function of the expected oscillation frequencies calculated from Eq. (2) for the $X\,^3\Pi$ and $^1\Pi$ states (see Table II). The major features of the data are in good agreement with the expected positions especially for the $X\,^3\Pi$ state. As was the case for oxygen in Fig. 7, vibrational resolution along the expected line for this state is clear, although in this case, the resolution comes from good experimental resolution in energy not in frequency. The data show a split line around the expected location of the $X\,^3\Pi$ line [see Eq. (3)], which could be due to saturation effects in the center of this line in Fig. 10(b). That is, the center of the line may be missing. We note that the revival time can also be obtained from a spectrum, such as Fig. 10(b): it is the reciprocal of the frequency spacing between any two adjacent islands.

We point out that the process, whereby oscillations in the dication states can be revealed in the pump-probe, even when the final observed molecule is also a dication, must be different from that previously reported for states in the oxygen dication [9]. In that case, a dication produced by the pump was further promoted by the probe to a triply charged molecule. In the present case [process (2) above], the charge state of the dication is not changed by the probe. All three lowest-lying wells in the dication of CO reach dissociation by predissociating through crossings with the $^3\Sigma^-$ state. We believe that the presence of the probe might influence this crossing when it arrives at the same time as the wave packet, thereby modulating the yield of dissociation products with the oscillatory period of the wave packet. No change in charge is required, just a change in dissociation yield.

The lower KER group, up to about 1 eV in Fig. 8, displays a vibrationally resolved structure similar to that discussed above for oxygen. This structure is shown in a blowup of the projected KER spectrum for this region in Fig. 11. Similar to oxygen, we believe these are generated by single- (or perhaps double-) photon absorption from bound wells in the cation. There are three main candidate wells (see Fig. 9), the $X\,^2\Sigma^+$, the $A\,^2\Pi$, and the $B\,^2\Sigma^+$, formed by extraction of an electron from the HOMO, the HOMO-1, and the HOMO-2 of the neutral one, respectively. While extraction of the HOMO is certainly the most probable, it is difficult to subsequently dissociate states from this well because it is so tightly bound. Indeed, it is quite probable that the yield of low-KER ions, from the

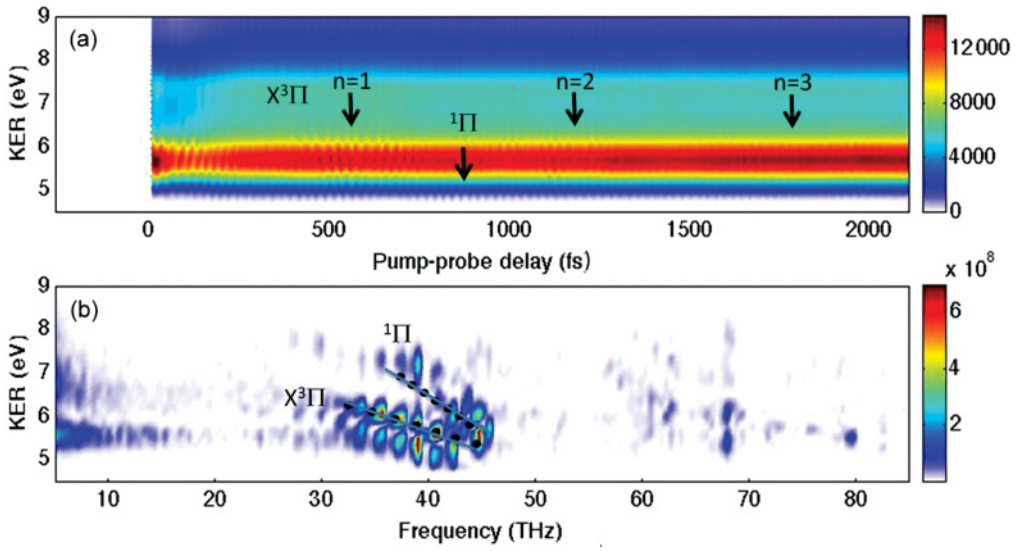

FIG. 10. (Color online) (a) Higher KER region for the observation of C^+ ions as a function of delay τ. Here, n represents the order of revivals. (b) Power spectrum of (a). The solid dots are calculated from the properties of states of the dication as shown in Table II. The short line segments are from Eq. (3), evaluated for $\nu = 1$.

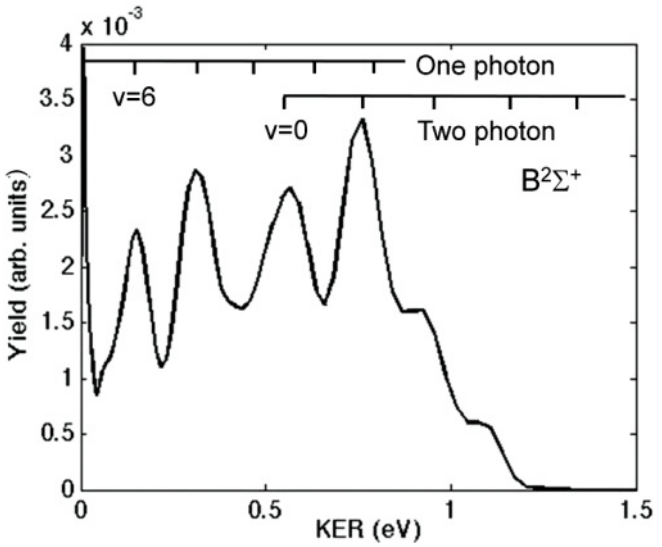

FIG. 11. Blowup of the low-KER region of Fig. 8. The locations of the expected KER from one- and two-photon absorption from vibrational states in the $B\,^2\Sigma^+$ well are shown.

dissociation of the cation of many molecules, originates not from initial HOMO extraction, but from HOMO-1 or even HOMO-2 extraction, since the production of the higher-lying states often places them near enough to the continuum that one (of a few) additional photons may bond soften the molecule into fragmentation [45]. In this case, we believe the low-KER ions we observe, come from extraction of the HOMO-1 or HOMO-2, that is, the $A\,^2\Pi$ and $B\,^2\Sigma^+$ states. The angular distribution of low-KER ions from the fragmentation of CO by extremely short (5-fs) low-intensity pulses suggests that, at least, the HOMO-1 must be in play and may be the HOMO-2 as well [46,47]. These studies also saw evidence of the vibrational structure we see in Fig. 11.

Figure 12(a) shows a blowup of the KER vs τ for this low-KER group with the power spectrum in Fig. 12(b). Again, the product of the mean-oscillation time (near 19 fs) with the energy spacing (near 0.21 eV) is close to Planck's constant, suggesting that the oscillations and the energy peaks are two manifestions of the same physical beating process. We suggest a process similar to that discussed above for oxygen. The expected frequencies for the $B\,^2\Sigma^+$ state appear to fit the observations best. While this should be the most difficult of the three wells for the pump to reach, it is the easiest one for the probe to promote for dissociation, and it is not unreasonable that this should be the one most visible. The highest frequency expected for the $A\,^2\Pi$ state is 45.8 THz, even for the ground vibrational state, clearly inconsistent with the measured frequencies. The $X\,^2\Sigma^+$ state can support oscillation frequencies up to 66 THz, but to dissociate this state from a vibrational state, which can yield a frequency as high as 52 THz, would require the absorption of at least three photons, and the accumulated bandwidth would be expected to remove any ability to see vibrational resolution.

Although it is the best candidate, the $B\,^2\Sigma^+$ state also comes with some interpretation problems. Figure 12(b) shows the expected locations of the frequencies as dots and the associated KER expected if a single photon is absorbed to dissociate the state to the lowest limit. The lowest vibrational state to yield a positive KER is $\nu = 6$ (see Table II). As was the case for oxygen, the predicted frequencies were somewhat lower than those observed. For comparison, in Fig. 12(b), we show the KER and frequencies expected if two photons were absorbed from the probe. While the agreement with the data is better, we doubt that this process is really responsible, since again, the question would arise, where is the single-photon process? There is some indication of oscillatory action near 62 THz, which is probably due to the $X\,^2\Sigma^+$ state, although we have no specific proposal for how this state should dissociate with very low KER.

It is clear from the low-KER data for both oxygen and carbon monoxide that something is missing in the interpretation. The basic problem is that the predicted oscillation frequencies seem lower than those observed. There are several possible sources for this discrepancy. First, by tightening up the PECs for both cases (making the spring constant greater), it would

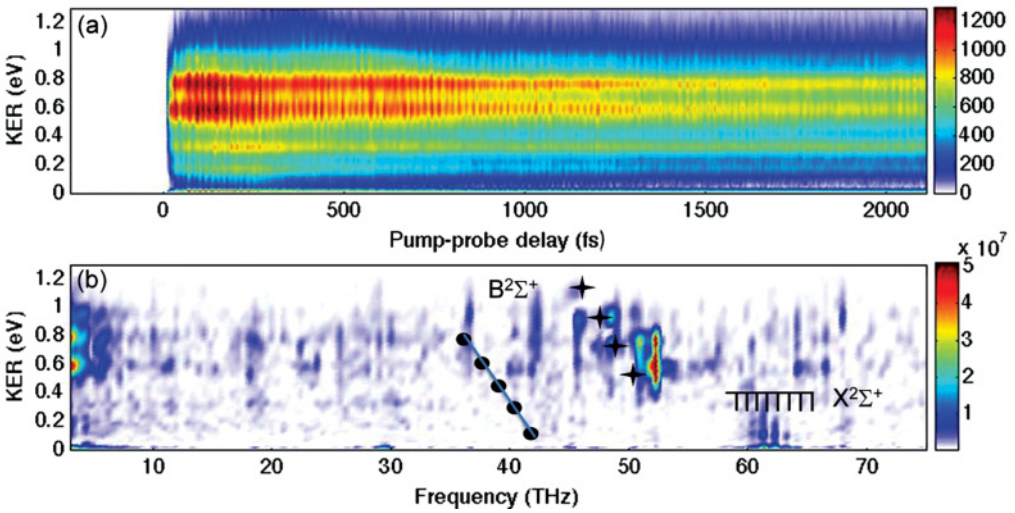

FIG. 12. (Color online) (a) Density plot of yield vs KER and τ for the low-KER region of Fig. 8. (b) Corresponding power spectrum. The short line segment is from Eq. (3), evaluated for $\nu = 6$.

be possible to achieve much better agreement between the data and the predicted loci in the oscillation frequency or KER map. We know of no justification for this, however. Most of the wave-packet motion occurs when no laser field is present, and thus, it seems unlikely that perturbation of the PEC by the laser is the source of the problem. By assuming two- or three-photon processes, which bring lower vibrational quantum numbers into play, agreement with the data is improved. However, we do not know why the one-photon process would not also be present and even be stronger in the spectra. There is no indication for both one- and two-photon processes. Furthermore, the observation of the vibrational energy structure relies on a narrow photon bandwidth. For a single-photon process, an 8-fs pulse has a bandwidth of ± 0.26 eV, which is already sufficient to considerably wash out vibrational spacings, which are at the 0.1–0.2-eV level. The more photons absorbed, the larger the bandwidth. It is possible that our ability to see a sharp energy structure with a nominal 8-fs pulse may be due to a pedestal of a few percent under the pulse, which could easily extend to 30 fs or more. In this case, one is performing a kind of long-pulse and short-pulse experiment at the same time. Finally, if we were at liberty to arbitrarily add about 1.2 eV to the KER we calculate from energy conservation, we would again bring the lower vibrational states, with their higher oscillation frequencies, into play and would improve agreement with the data. We know of no justification for doing this, either.

IV. THEORETICAL TREATMENT OF QUANTUM DYNAMICS ON COUPLED ADIABATIC POTENTIAL CURVES

The interpretations given above are based on simplified models and assumptions about the time-evolution of complex quantum systems on the edge of the uncertainty principle. Major interpretation problems emerge. In this section, we attempt to probe the model much more deeply by a full solution, within a restricted basis, of the time-dependent Schrödinger equation (TDSE) for the nuclear motion in the oxygen system. We present a general discussion of a theoretical treatment of wave packets launched by a pump pulse onto a manifold of excited potential curves that are subsequently coupled by a delayed probe pulse. We then apply this approach to the $a\ ^4\Pi_u/f\ ^4\Pi_g$ two-state coupling in the O_2^+ molecular ion discussed qualitatively above.

A. Single-curve calculations

Following the single or multiple ionization of the neutral diatomic molecule in an ultrashort few-cycle IR pump laser pulse, we study the effect of nonadiabatic couplings on the dissociation dynamics of the singly or multiply charged molecular ion in a second delayed femtosecond IR probe laser pulse. Since the pump pulse typically generates a molecular ion in a superposition of electronic and vibrational states, we first attempt to identify electronic states that participate in the dissociation dynamics by examining the dynamics of a nuclear wave packet separately on given individual adiabatic potential curves $V_i(R)$ of the molecular ion. Assuming pump-probe delays τ, which are short on the time scale of the molecular rotation, we neglect molecular rotation and rovibrational couplings [48] and solve the one-dimensional time-dependent Schrödinger equation (using atomic units unless indicated otherwise),

$$i\frac{d}{dt}\psi_i = [T_R + V_i(R)]\psi_i, \tag{4}$$

where T_R is the operator for the kinetic energy of the relative nuclear motion.

We model the initial ionization of the ground-state neutral molecule in the electric field of the pump pulse in the FC approximation in order to obtain the initial nuclear wave packet in the molecular ion,

$$\psi_i(R,t=0) = \sum_\nu a_{i,\nu}\varphi_{i,\nu}(R), \tag{5}$$

in terms of the FC amplitudes $a_{i,\nu}$ [32]. The index ν designates vibrational states $\varphi_{i,\nu}$ in the ith bonding adiabatic electronic state of the molecular ion with vibrational energies $\omega_{i,\nu}$. By numerical wave-packet propagation of Eq. (4), subject to the initial condition (5), we obtain the field-free evolution of Eq. (5), $\psi_i(R,t)$. Repeating these calculations for several selected potential energy curves, we identify the relevant electronic states by comparing characteristics of the bound wave-packet motion in $V_i(R)$, such as vibrational periods T_i and full and partial revival times $T_{\mathrm{rev,i}}$ [15] with pump-probe-delay-dependent measured KER data [9,20]. (In this particular application, we restrict ourselves to a single value of i, corresponding to the $a\ ^4\Pi_u$ state.)

B. Coupled adiabatic potential curves

Modeling the coherent motion of nuclear vibrational wave packets on several FC-populated adiabatic potential curves of the diatomic molecular ion, we allow for dipole couplings D_{ij} of (individually launched) nuclear wave packets ψ_i and ψ_j in the electric field of the probe laser pulse by numerically propagating the coupled TDSE [22,32],

$$i\frac{d}{dt}\begin{pmatrix}\psi_1\\ \psi_2\\ \vdots\end{pmatrix} = \begin{pmatrix}T_R+V_1 & D_{12} & \cdots\\ D_{21} & T_R+V_2 & \cdots\\ \vdots & \vdots & \ddots\end{pmatrix}\begin{pmatrix}\psi_1\\ \psi_2\\ \vdots\end{pmatrix}. \tag{6}$$

(In this particular example, we only allow coupling of the $a\ ^4\Pi_u$ to the $f\ ^4\Pi_g$; that is, the above matrix is 2×2.) In order to simulate the KER spectra, we numerically propagate Eq. (6) for a sufficiently long time $t_{\max}$, including field-free propagation of the nuclear wave packets up to a time of typically $\sim$100 fs after the action of the probe pulse. For each pump-probe delay τ, the bound and dissociating parts of the nuclear motion at time $t_{\max}$ can be separated in terms of the internuclear distance R_1 (typically about 4 a.u.) such that the probability current associated with the dissociation of the molecular ion has no relevant contributions for $R < R_1$. Fourier transformation of the dissociating parts of the nuclear wave packets over the interval $[R_1, R_{\max}]$ then yields the momentum representations of the dissociating wave packets,

$$\tilde{\psi}_i^{\mathrm{diss}}(P,t_{\max}) = \int_{R_1}^{R_{\max}} dR\,\psi_i(R,t_{\max})e^{-iPR}, \tag{7}$$

where $R_{\max}$ (typically about 40 a.u. in our calculations) is related to the size of the numerical grid. By incoherently adding the momentum distributions from all electronic states (two in this case), we obtain the pump-probe-delay-dependent distribution of fragment KERs, E_k,

$$C^{\rm diss}(E_k,\tau) \propto \sum_i \left|\tilde{\psi}_i^{\rm diss}(P,t_{\max})\right|^2 \Big/ P. \tag{8}$$

For homonuclear molecules, $E_k = P^2/m$. The KER is twice the single-ion energy. Subtracting the delay-independent background $C^{\rm diss}_{\rm incoh} = \frac{1}{T}\int_0^T d\tau\, C^{\rm diss}(E_k,\tau)$, we obtain the power spectrum,

$$P^{\rm diss}(E_k,f) = \left| \int_0^{\rm T} d\tau \left[C^{\rm diss}(E_k,\tau) - C^{\rm diss}_{\rm incoh}(E_k)\right] e^{-i2\pi f\tau} \right|^2. \tag{9}$$

We apply this formalism to the $a\,^4\Pi_u/f\,^4\Pi_g$ two-state case. We employed the General Atomic and Molecular Electronic Structure System (GAMESS) quantum chemistry code [49] to obtain the PECs and dipole matrix elements. The calculated KERs (8), as a function of the delay, and the corresponding power spectrum (9), as a function of the beat frequency f, are shown in Figs. 13(a) and 13(c), respectively, for a probe-pulse intensity of 3×10^{14} W/cm^2 and a pulse duration of 15 fs. (This pulse length is longer than the experimental one but gives a spectrum more nearly resembling the data.)

The negative slope of the KER near ~26 and ~30 THz in Figs. 13(c) and 13(d) can be interpreted as the combined effect of the anharmonicity of the PEC (leading to smaller vibrational energy spacings and, thus, smaller quantum-beat frequencies at larger vibrational energies) and the distortion of the molecular electronic state in the electric field of the probe laser (AC Stark shift). The Stark shift in the field of the probe laser tends to lower the electronic energy of the molecule at larger internuclear distances, leading to increasing shifts to lower energies of the vibrational energy levels $\omega_{i,\nu}$ for increasing vibrational quantum numbers ν [21]. This probe-induced shift, therefore, tends to further enhance the anharmonicity-related decrease in the vibrational level spacings, i.e., the quantum-beat frequencies in Fig. 13(c), thereby worsening the agreement with the measured data in Fig. 13(d). However, since the O_2^+ vibrational wave packet mostly propagates freely and for the (assumed) short-probe pulses considered in this paper, probe-induced level shifts are negligible.

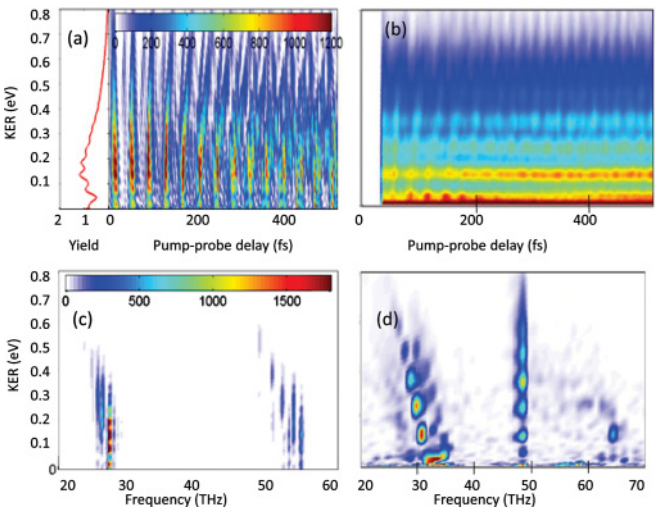

FIG. 13. (Color online) Calculated (a) and (c) and measured (b) and (d) KER spectra for O_2^+ as a function of (a) and (b) pump-probe delay and (c) and (d) frequency. Calculated KER spectra include dipole coupling of the $a\,^4\Pi_u$ and $f\,^4\Pi_g$ states by the 15-fs probe laser pulse with 3×10^{14}-W/cm^2 peak intensity. The power spectra (c) and (d) are obtained with a sampling time of 2 ps (see text).

Comparison with the experimental results in Figs. 13(b) and 13(d) shows that several features of the experimental data are reproduced. The oscillatory structure, with a period near 38 fs, is seen, similar but not equal to the experimental period near 34 fs. The observed frequencies in the power spectrum are correspondingly lower than the experimental ones by about 25%. The systematic forward tilting of the lines with increasing τ, seen in the data of Fig. 13(b), is reproduced. This behavior also appears in the power spectrum as a negative slope in the plot of the KER vs frequency. What appears to be vibrational structure appears in the projection of the spectrum of Fig. 13(a) onto the KER axis in apparent agreement with the experimental result. However, close examination shows this comparison to be somewhat misleading: The spacing of the vibrational peaks in Fig. 13(a) is about half that observed in the experiment, and the power spectrum shows that, for each discrete frequency, a range of KER energies is produced, not the nearly single-valued peaks seen in the experiment.

Modeling the pump process in FC approximation, our simulation does not account for the nuclear wave-packet motion in the neutral molecule. It, therefore, neglects possible "Lochfrass" effects [39], which we had tentatively related to the strong group near 49 THz in Fig. 13(d), based on the speculation that the probe pulse might be capable of both ionizing the neutral molecule and dissociating O_2^+ by coupling of its $a\,^4\Pi_u$ and $f\,^4\Pi_g$ electronic states (see Sec. III B above). A significantly larger than anticipated temporal width of the pump and probe pulses would tend to support this hypothesis but would worsen the agreement between calculated and measured O_2^+ quantum-beat frequencies.

There are numerous difficulties that the calculation is expected to encounter when asked to reproduce the experiment. These include the omission of volume intensity integration, the inclusion of a possible few-percent pedestal extending up to as much as 100 fs on the short pulse, and the role of other ignored channels. Qualitatively, the calculation reproduces the main features of the data; quantitatively, it falls short, more or less on the same points as the simpler arguments discussed in earlier sections. Nevertheless, we believe that the fundamental process has been correctly identified, and this is confirmed by the calculation.

V. CONCLUSION AND SUMMARY

We have performed pump-probe explorations of the behavior of both dissociative and (quasi) bound wave packets launched and probed by 8-fs IR pulses for nitrogen, oxygen,

and carbon monoxide. The dissociative trajectories in the KER-τ space can be identified using a simple Coulomb model for the PECs, but we do not attempt to extract further information, such as identification of the specific states involved, from the data. The real-time dynamics of the bound-state wave packets is revealed by rich beating structures characterized by oscillatory motion and vibrational revivals. By using power spectra (Fourier transform of the time spectrum as a function of the KER), the oscillatory frequencies are found to be correlated with the KER. By using both the time and the frequency data, the time-dependent motion can, in several cases, be assigned to motion in specific PECs.

For the cases of oxygen and carbon monoxide, low-energy KER features are found, which display both vibrational structure in the energy structure and oscillatory structure in the time domain. The product of the vibrational energy spacing and the period of oscillation is found to be near Planck's constant, suggesting that we are observing the same wave-packet motion in both the time and the energy domains. Specific mechanisms are suggested for the creation (pump) and subsequent fragmentation (probe) for these features. For these mechanisms, we calculate expected locations of the KER values and associated oscillation frequencies for different vibrational states participating in the wave-packet motion. It is predicted that, in KER-frequency space, islands should appear along a line with a well-defined slope, and vibrational resolution can be obtained by high resolution in either the KER or the frequency. For the cases of the low-energy ions from the cations of oxygen and carbon monoxide, the experimental resolution is adequate to resolve the islands in both the KER and the frequency. For the dication of carbon monoxide, similar islands are seen, but the vibrational resolution comes only because the frequency resolution is sufficient.

The data are in excellent agreement with expectations of the simple model for the dication of carbon monoxide. For the low-energy ions from the cation of both oxygen and carbon monoxide, the data are in general qualitative agreement with the model, but quantitative puzzles remain. The full solution to the Schrödinger equation for the oxygen cation case is again in qualitative but not quantitative agreement with the data. Indeed, when plotted in the KER-frequency space (the power spectra), the experimental data appear to be cleaner and more striking than the results of the calculation, a very unusual situation. It is usually the other way around: the lack of control of some parameter in the real experimental world usually makes the result uglier than the theoretical result, which is under better control. It is possible that there is still some conceptual default in our simple model, but we have not been able to identify it. Nevertheless, we believe that time-dependent measurements, such as these, open up new avenues for the study of molecular dynamics of nonstationary states with implications for both the structure and the dynamics of the molecules involved. In particular, the observation of the same dynamics in both time and energy domains in a single pump-probe experiment has not been reported.

ACKNOWLEDGMENTS

This work was supported by the Chemical Sciences, Geosciences, and Biosciences Division, Office of Basic Energy Sciences, Office of Science, US Department of Energy, the National Science Foundation under Grant No. CHE-0822646 and the DFG via the Emmy-Noether program, the International Collaboration in Chemistry program, and the Cluster of Excellence: Munich Center for Advanced Photonics (MAP).

[1] A. H. Zewail, Science **242**, 1645 (1988).
[2] T. Ergler, A. Rudenko, B. Feuerstein, K. Zrost, C. D. Schröter, R. Moshammer, and J. Ullrich, Phys. Rev. Lett. **97**, 193001 (2006).
[3] F. Légaré, K. F. Lee, I. V. Litvinyuk, P. W. Dooley, A. D. Bandrauk, D. M. Villeneuve, and P. B. Corkum, Phys. Rev. A **72**, 052717 (2005).
[4] A. S. Alnaser *et al.*, Phys. Rev. A **72**, 030702(R) (2005).
[5] H. Niikura, D. M. Villeneuve, and P. B. Corkum, Phys. Rev. A **73**, 021402(R) (2006).
[6] F. Kelkensberg *et al.*, Phys. Rev. Lett. **103**, 123005 (2009).
[7] L. Fang and G. N. Gibson, Phys. Rev. A **81**, 033410 (2010).
[8] L. Fang and G. N. Gibson, Phys. Rev. Lett. **100**, 103003 (2008).
[9] S. De, I. A. Bocharova, M. Magrakvelidze, D. Ray, W. Cao, B. Bergues, U. Thumm, M. F. Kling, I. V. Litvinyuk, and C. L. Cocke, Phys. Rev. A **82**, 013408 (2010).
[10] A. T. J. B. Eppink and D. H. Parker, Rev. Sci. Instrum. **68**, 3477 (1997).
[11] L. Dinu, A. T. J. B. Eppink, F. Rosca-Pruna, H. L. Offerhaus, W. J. van der Zande, and M. J. J. Vrakking, Rev. Sci. Instrum. **73**, 4206 (2002).
[12] M. J. J. Vrakking, Rev. Sci. Instrum. **72**, 4084 (2001).
[13] I. A. Bocharova, A. S. Alnaser, U. Thumm, T. Niederhausen, D. Ray, C. L. Cocke, and I. V. Litvinyuk, Phys. Rev. A **83**, 013417 (2011).
[14] S. Voss, A. S. Alnaser, X.-M. Tong, C. Maharjan, P. Ranitovic, B. Ulrich, B. Shan, Z. Chang, C. D. Lin, and C. L. Cocke, J. Phys. B. **37**, 4239 (2004).
[15] R. W. Robinett, Phys. Rep. **392**, 1 (2004).
[16] A. Zavriyev, P. H. Bucksbaum, H. G. Muller, and D. W. Schumacher, Phys. Rev. A **42**, 5500 (1990).
[17] A. Giusti-Suzor, X. He, O. Atabek, and F. H. Mies, Phys. Rev. Lett. **64**, 515 (1990).
[18] S. Chelkowski, P. B. Corkum, and A. D. Bandrauk, Phys. Rev. Lett. **82**, 3416 (1999).
[19] B. Feuerstein and U. Thumm, Phys. Rev. A **67**, 063408 (2003).
[20] B. Feuerstein, T. Ergler, A. Rudenko, K. Zrost, C. D. Schröter, R. Moshammer, J. Ullrich, T. Niederhausen, and U. Thumm, Phys. Rev. Lett. **99**, 153002 (2007).
[21] U. Thumm, T. Niederhausen, and B. Feuerstein, Phys. Rev. A **77**, 063401 (2008).
[22] M. Magrakvelidze, F. He, T. Niederhausen, I. V. Litvinyuk, and U. Thumm, Phys. Rev. A **79**, 033410 (2009).
[23] R. J. Gdanitz, Chem. Phys. Lett. **283**, 253 (1998).

[24] A. Ehresmann *et al*., J. Phys. B **39**, 283 (2006).
[25] M. Lundqvist, D. Edvardsson, P. Baltzer, and B. Wannberg, J. Phys. B **29**, 1489 (1996).
[26] P. W. Dooley, I. V. Litvinyuk, K. F. Lee, D. M. Rayner, M. Spanner, D. M. Villeneuve, and P. B. Corkum, Phys. Rev. A **68**, 023406 (2003).
[27] S. R. Langhoff, C. W. Bauschlicher, and H. Partridge, J. Chem. Phys. **87**, 4716 (1987).
[28] G. Dawber, A. G. McConkey, L. Avaldi, M. A. MacDonald, G. C. King, and R. I. Hall, J. Phys. B **27**, 2191 (1994).
[29] K. P. Huber and G. Herzbert, *Molecular Spectra and Molecular Structure: Contants of Diatomic Molecules* (Van Nostrand-Reinhold, New York, 1979).
[30] B. Wannberg, D. Nordfors, K. L. Tan, L. Karlsson, and L. Mattsson, J. Electron. Spectrosc. Relat. Phenom. **47**, 147 (1988).
[31] M. Lundqvist, P. Baltzer, D. Edvardsson, L. Karlsson, and B. Wannberg, Phys. Rev. Lett. **75**, 1058 (1995).
[32] T. Niederhausen and U. Thumm, Phys. Rev. A **77**, 013407 (2008).
[33] D. Pavičić, T. W. Hänsch, and H. Figger, Phys. Rev. A **72**, 053413 (2005).
[34] P. Q. Wang, A. M. Sayler, K. D. Carnes, J. F. Xia, M. A. Smith, B. D. Esry, and I. Ben-Itzhak, Phys. Rev. A **74**, 043411 (2006).
[35] J. McKenna, A. M. Sayler, B. Gaire, N. G. Johnson, M. Zohrabi, K. D. Carnes, B. D. Esry, and I. Ben-Itzhak, J. Phys. B **42**, 121003 (2009).
[36] V. S. Prabhudesai *et al*., Phys. Rev. A **81**, 023401 (2010).
[37] M. Zohrabi *et al*., Phys. Rev. A **83**, 053405 (2011).
[38] C. M. Marian, R. Marian, S. D. Peyerimhoff, B. A. Hess, R. J. Buenker, and G. Seger, Mol. Phys. **46**, 779 (1982).
[39] T. Ergler, B. Feuerstein, A. Rudenko, K. Zrost, C. D. Schröter, R. Moshammer, and J. Ullrich, Phys. Rev. Lett. **97**, 103004 (2006).
[40] T. Osipov *et al*., Phys. Rev. A **81**, 011402 (2010).
[41] T. Šedivcová, P. R. Žd'ánská, V. Špirko, and J. Fišer, J. Chem. Phys. **124**, 214303 (2006).
[42] T. Šedivcová-Uhlíková, P. R. Kaprálová-Žd'ánská, and V. Špirko, Int. J. Quantum Chem. **107**, 2654 (2007).
[43] P. Baltzer, M. Lundqvist, B. Wannberg, L. Karlsson, M. Larsson, M. A. Hayes, J. B. West, M. R. F. Siggel, A. C. Parr, and J. L. Dehmer, J. Phys. B **27**, 4915 (1994).
[44] S. Hsieh and J. H. D. Eland, J. Phys. B **29**, 5795 (1996).
[45] H. Akagi, T. Otobe, A. Staudte, A. Shiner, F. Turner, R. Dörner, D. M. Villeneuve, and P. B. Corkum, Science **325**, 1364 (2009).
[46] I. Znakovskaya, P. von den Hoff, S. Zherebtsov, A. Wirth, O. Herrwerth, M. J. J. Vrakking, R. de Vivie-Riedle, and M. F. Kling, Phys. Rev. Lett. **103**, 103002 (2009).
[47] P. von den Hoff, I. Znakovskaya, S. Zherebtsov, M. F. Kling, and R. de Vivie-Riedle, Appl. Phys. B **98**, 659 (2010).
[48] M. Winter, R. Schmidt, and U. Thumm, Phys. Rev. A **80**, 031401(R) (2009); New J. Phys. **12**, 023020 (2010).
[49] M. S. Gordon and M. W. Schmidt, in *Theory and Applications of Computational Chemistry, the first 40 years*, edited by C. E. Dykstra, G. Frenking, K. S. Lim, and G. E. Scusaria (Elsevier, Amsterdam, 2005).